Journal of Materials Chemistry A

ROYAL SOCIETY OF CHEMISTRY

PAPER

View Article Online
View Journal

Cite this: DOI: 10.1039/d2ta06458h

The "burst effect" of hydrogen desorption in MgH_2 dehydrogenation†

Shuai Dong,[ab] Chaoqun Li,[ab] Jinhui Wang,[ab] Hao Liu,[ab] Zhao Ding,[c] Zhengyang Gao,[ab] Weijie Yang, *[ab] Wei Lv,[de] Li Wei, [f] Ying Wu*[de] and Hao Li *[g]

Magnesium hydride (MgH_2) is a promising material for solid hydrogen storage due to its superior hydrogen storage capacity. However, its commercial application is inhibited by the sluggish dehydrogenation kinetics resulting from the complex hydrogen migration and desorption processes. Herein, we study the sequential MgH_2 dehydrogenation mechanism by analyzing the kinetic and structural changes during the layer-by-layer hydrogen desorption process. Our results obtained by spin-polarized density functional theory calculations with van der Waals corrections (DFT-D3) unveiled an interesting "burst effect" during MgH_2 dehydrogenation. We found that the initial dehydrogenation barriers (2.52 and 2.53 eV) are much higher than the subsequent reaction barriers (0.12–1.51 eV). The Mg–H bond analyses by the crystal orbital Hamilton population method indicate that the Mg–H bond strength decreases along the dehydrogenation process. Therefore, the subsequent H migration and hydrogen desorption become significantly easier, showing a "burst effect". Electronic structure analyses using the electron localization function show that the H vacancy still has a high degree of electronic localization when the first layer of atomic H exists. Furthermore, *ab initio* molecular dynamics simulations were performed to analyze the kinetic characteristics of MgH_2 after surface dehydrogenation to provide more evidence. This identified burst effect provides a theoretical basis for the dehydrogenation kinetics of MgH_2 and proposes important guidelines for modifying MgH_2-based hydrogen storage materials: promoting the initial dehydrogenation by structural engineering could be the key to facilitating the hydrogen desorption of MgH_2.

Received 16th August 2022
Accepted 16th September 2022

DOI: 10.1039/d2ta06458h

rsc.li/materials-a

1 Introduction

Hydrogen energy has become the focus of energy research in recent years due to its abundant resources and zero pollution.[1,2] However, the application of hydrogen energy has been limited by its storage and transportation. Currently, hydrogen can be stored by three methods: high-pressure gaseous hydrogen storage, low-temperature liquid hydrogen storage, and solid-state hydrogen storage among which solid-state materials generally have the highest safety and hydrogen storage density.[3]

In recent years, various hydrogen storage materials have emerged, such as lightweight metal hydrides[4–6] and carbon-based hydrogen materials.[7,8] MgH_2, as a type of metal hydride, has been widely studied due to its low cost and high hydrogen storage capacity.[9–12] However, its high dehydrogenation enthalpy (76 kJ mol^{-1}) has hampered its industrial applications.[13,14] Experimental results indicated some effective methods, including generating MgH_2 nanoparticles directly by direct or doped mechanical milling,[15–19] activating the material by alloying,[20,21] and lowering the activation barriers by doping catalysts.[22–25] Liang *et al.*[15] proposed a strategy to lower the hydrogen desorption barrier to 62 kJ mol^{-1} by mechanical milling of MgH_2 with V. In terms of alloying and doping catalysts, Vajo and co-workers[20] reported that the dehydrogenation energy barrier was reduced to 36.4 kJ mol^{-1} on a MgH_2/Si system. Yu *et al.*[25] calculated that the dehydrogenation barrier of a MgH_2/BCC ($Ti_{0.4}Cr_{0.15}Mn_{0.15}V_{0.3}$ alloy) mixture was 71.2 ± 5 kJ mol^{-1}.

In mechanism interpretation and materials design, many studies employed vacancy engineering. Dai *et al.*[26,27] used first

[a]School of Energy and Power Engineering, North China Electric Power University, Baoding, 071003, Hebei, China. E-mail: yangwj@ncepu.edu.cn

[b]Hebei Key Laboratory of Low Carbon and High Efficiency Power Generation Technology, North China Electric Power University, Baoding, 071003, Hebei, China

[c]College of Materials Science and Engineering, Chongqing University, Chongqing, 400044, China

[d]Advanced Energy Materials Research Institute, North China Electric Power University, No. 2 Beinonglu, Changping District, Beijing, 102206, China. E-mail: yingwu2000@hotmail.com

[e]Central Iron & Steel Research Institute, Advanced Technology & Materials Co., Ltd, No. 76 Xueyuannanlu, Haidian District, Beijing, 100081, China

[f]School of Chemical and Biomolecule Engineering, The University of Sydney, Darlington 2006, NSW, Australia

[g]Advanced Institute for Materials Research (WPI-AIMR), Tohoku University, Sendai 980-8577, Japan. E-mail: li.hao.b8@tohoku.ac.jp

† Electronic supplementary information (ESI) available. See https://doi.org/10.1039/d2ta06458h

principles calculations to analyze the dehydrogenation properties of Al-, Ti-, Mn-, and Ni-doped Mg vacancies on MgH_2 (110) and (001). German *et al.*[28,29] studied the effects of Zr- and Nb-doping and vacancies on the hydrogen desorption properties of MgH_2 (001) and (110); they found that doping and vacancy engineering can promote hydrogen desorption. Similarly, by analyzing the structure after doping and hole formation, near-surface vacancies were found to have a predominant effect on lowering the hydrogen desorption temperature.[30] However, there are very few studies focusing on the vacancy concentration. Chen *et al.*[31] analyzed the formation of surface H vacancies on MgH_2 (110), (100), (101), and (001) and found that dehydrogenation is even easier with an increase in the H vacancy concentration. However, to the best of our knowledge, there was no kinetic-based analysis of the formation process of H vacancies and the effects of vacancy concentrations on hydrogen desorption. Though some previous studies analyzed how dehydrogenation behaves on MgH_{2-x} with partial holes or doped partial holes,[26–31] the actual situation should be much more complicated – we should consider not only the reduction of surface H, but also the reduction of internal H. The lack of a complete landscape of MgH_2 dehydrogenation still severely restricts the development of hydrogen storage materials.

Herein, first principles calculations were employed to comprehensively study the dehydrogenation processes of MgH_2, including H migration and hydrogen desorption. According to previous studies,[32] MgH_2 (110) was the most stable and widely studied surface. Therefore, all MgH_2 surfaces in this study were modeled as stable (110) slabs. Then, the bonding strengths of Mg–H during dehydrogenation were calculated using the crystal orbital Hamilton population (COHP) method.[33,34] After this, electron localization functions (ELFs) were calculated to analyze the effects of dehydrogenation on the electron localization of subsequent structures. Finally, *ab initio* molecular dynamics (AIMD) simulations were employed to support the conclusions more quantitatively. We identified the main dehydrogenation steps that make MgH_2 (110) dehydrogenation difficult and explained the formation of an interesting burst effect, which provides optimization guidelines to promote the dehydrogenation of MgH_2-based materials in the future.

2 Computational and modeling methods

Density functional theory (DFT) calculations were performed using the Vienna *ab initio* simulation package (VASP) with the projector augmented wave (PAW) method.[35] Because the Perdew–Burke–Ernzerhof (PBE) functional was found to be relatively accurate for describing the adsorption and desorption of hydrogen based on previous benchmarking studies,[36] the PBE within the generalized gradient approximation (GGA) framework was employed in this study.[37–39] Van der Waals corrections were considered by using the DFT-D3 method in all the DFT calculations.[40] Spin polarization was also considered.[41] A 500 eV energy cutoff of the plane wave basis set was used to describe the valence electrons and a $(4 \times 4 \times 1)$ Γ-centered k-point grid was employed for structural relaxation (Fig. S1†). The simple harmonic oscillator (zero-point energy) and entropic change at 700 K were considered. Because the commercial MgH_2 dehydrogenation temperature is generally above 625 K,[42–44] 700 K was selected as the entropy reference temperature. The climbing-image nudged elastic band (Cl-NEB) method developed by Henkelman *et al.*[45,46] was employed to locate the transition states of the dehydrogenation reactions. The COHP method[33,34] was employed to analyze the bonding information using the LOBSTER package.[47,48] For the MgH_2 surface, we chose a large (4×1) surface unit cell, where a vacuum layer of more than 12 Å was applied to the z-direction. In this study, we used the Gibbs free energy for analysis (by considering the entropic change and zero-point energy). The Gibbs free energies were calculated as follows:

$$G = E_e + E_{ZPE} + \Delta TS \quad (1)$$

where G represents the Gibbs free energy, E_e represents the DFT calculated energy, E_{ZPE} represents the zero-point energy, and ΔTS represents the entropic change.

To determine the most favorable termination of MgH_2 (110),[32] we calculated the surface formation energies (σ) of three typical MgH_2 (110) surfaces (Table S1†); the structure with the lowest energy (Fig. 1a and S1b†) was selected as the structure used in the subsequent study. Herein, σ was calculated using the following equation:

$$\sigma = \left(E_{rel} + E_{slab} - \frac{N_{slab}}{N_{bulk}} \times E_{bulk}\right) \times \frac{1}{A}, \quad (2)$$

where E_{rel} is the energy change in the relaxation process, E_{slab} is the energy of the unrelaxed slab model, E_{bulk} is the molecular conventional cell energy, A is the exposed surface area, N_{slab} is the number of atoms in the slab model, and N_{bulk} is the number of protocell atoms. The AIMD simulation module embedded in the VASP code was employed with a time step of 1 fs, using the NVT ensemble with the Nose–Hoover thermostat. Geometries were considered relaxed when all the forces of each atom fell below 0.05 eV $Å^{-1}$. After AIMD simulations, we used the post-processing program VASPKIT[49] to obtain the mean square displacement (MSD) of the atom. The diffusion coefficient D was calculated from the MSD of H using:[50]

$$D = \lim_{t \to \infty} \left[\frac{1}{2dt} \left\langle [\vec{r}(t)]^2 \right\rangle\right], \quad (3)$$

where d is the dimension ($d = 3$), $\vec{r}(t)^2$ is MSD and t is simulation time. Previous studies[51] found that the activation energy (E_a) can be obtained from the diffusivity diagram with temperature:

$$D = A \exp\left(\frac{-E_a}{k_B T}\right), \quad (4)$$

where k_B is Boltzmann's constant, T is environmental temperature, and A is the prefactor.

3 Results and discussion

During dehydrogenation, hydrogen may desorb from the bulk layer by layer. To better explain this, we labelled the bridging H

in the upper three layers as red (first layer bridge H, FBH), green (second layer bridge H atom, SBH), and blue (third layer bridge H atom, TBH), respectively. The most favorable reaction path was determined by using the final state with the lowest energy. To distinguish the Mg–H bonds, we numbered them for the bonding analysis. We defined the bond position with A–B as shown in Fig. 1b, where A is the number of layers and B increases from left to right and from front to back. Based on the analysis, the dehydrogenation process can be divided into eight stages. Each layer was divided into several processes according to the independent dehydrogenation processes or continuous dehydrogenation. The dehydrogenation of the atomic H in the first layer includes Processes 1 and 2. The dehydrogenation of the atomic H in the second and third layers includes Processes 3–6 and 7 and 8, respectively. The atomic H involved in each process is labelled in blue, as shown in Fig. 1c. And the final structure of the dehydrogenation process was selected as a distinct lamellar structure, and then the lowest energy, *i.e.*, the most stable structure, was selected.

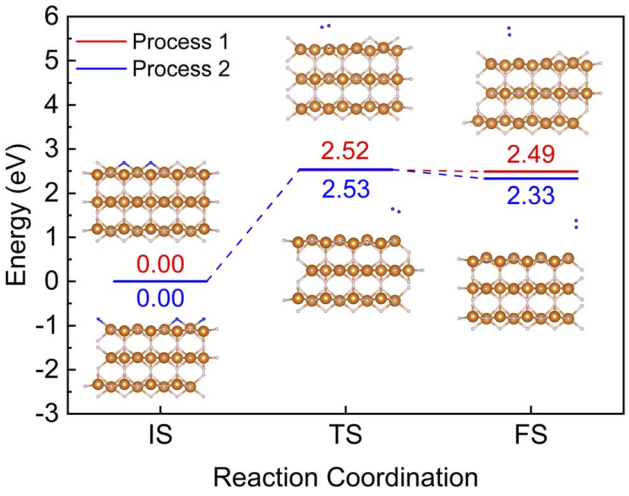

Fig. 2 Structure and energy changes of the first-layer atomic H during dehydrogenation. White and orange spheres represent H and Mg, respectively. Blue spheres represent the atomic H involved in the reaction.

3.1 The first layer

According to previous studies on surface dehydrogenation, double BH dehydrogenation was found to be a plausible reaction pathway.[32,52–54] Therefore, we chose this dehydrogenation path as the initial step. Then, the dehydrogenation path was calculated using the CI-NEB method (Fig. 2). For the dehydrogenation of FBH, the energy barrier in Process 2 (2.53 eV) is similar to that in Process 1 (2.52 eV). The layered structure of MgH_2 is also basically unchanged. These values are consistent with those in previous studies (*e.g.*, 2.37,[32] 2.21,[55] and 2.08 eV[56]). However, there is no obvious relationship between the dehydrogenation energy barrier and the quantity of surface H vacancies.

3.2 The second layer

Different from the first-layer dehydrogenation, the second-layer H need to migrate to the stable site in the first layer before desorption (Fig. 3). The hydrogen desorption barriers of the second layer (1.06–1.51 eV) are much lower than those of the

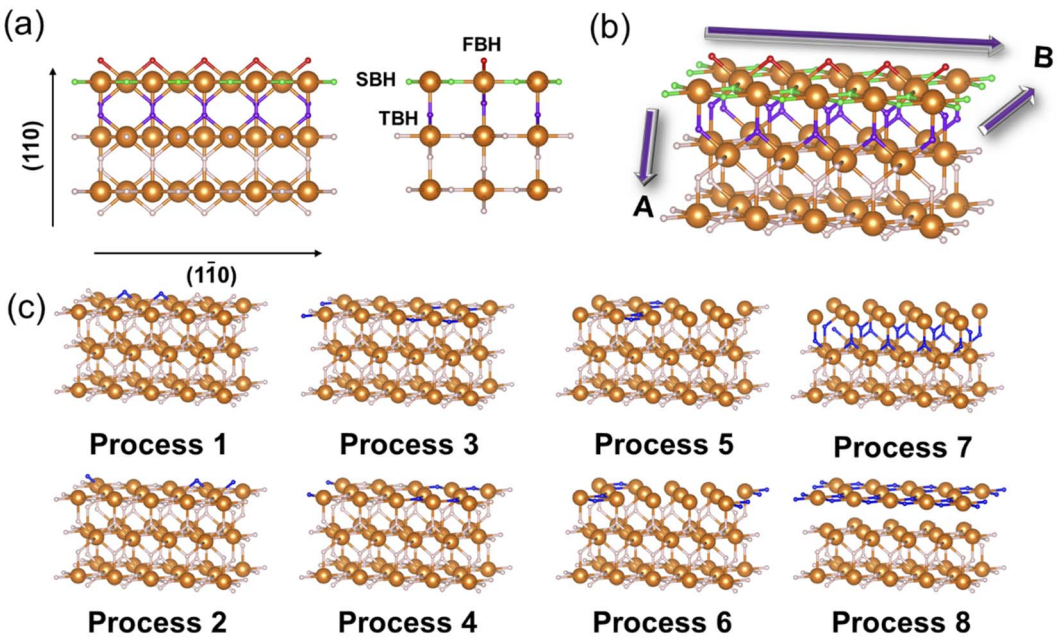

Fig. 1 (a) Front and top views of the MgH_2 (110) surface. White and orange spheres represent H and Mg, respectively. Red, green, and purple spheres represent the first, second, and third layers of atomic H, respectively. (b) Directional displays of the bonding position number. The direction of the arrow represents the increase of A and B. (c) The atomic H involved in the eight dehydrogenation processes (blue spheres).

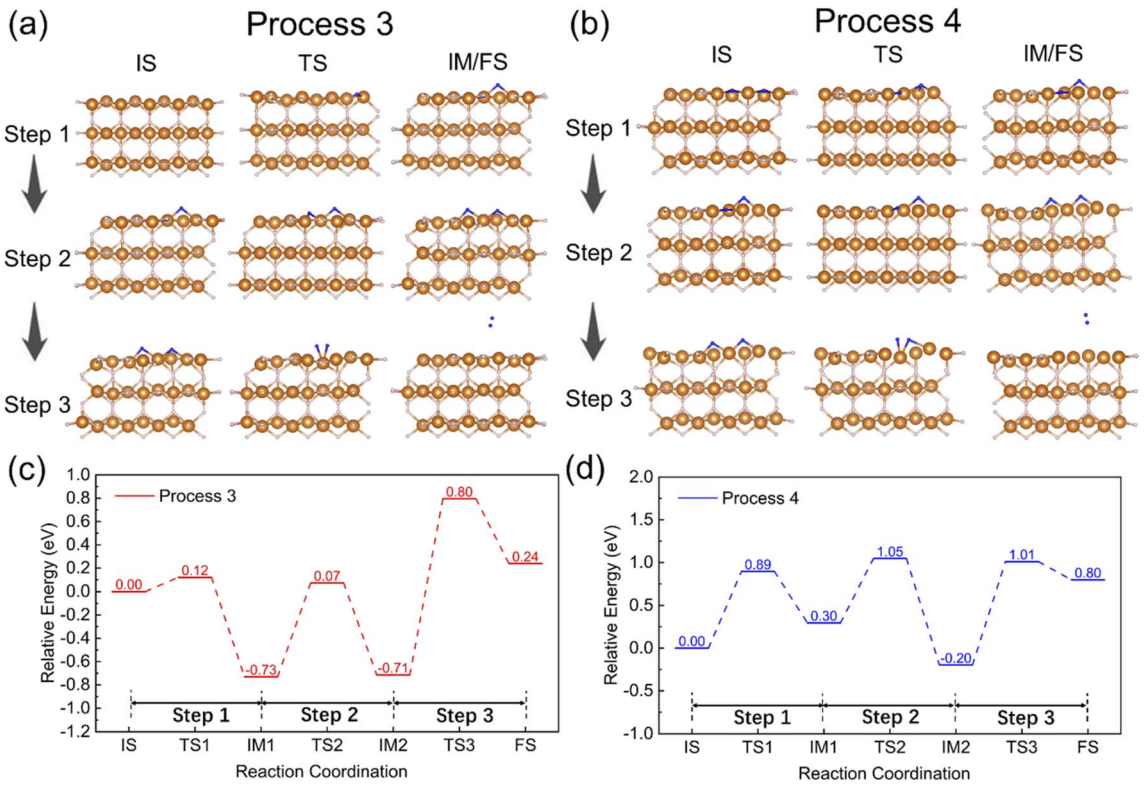

Fig. 3 (a and b) Structural changes of the second-layer atomic H during the dehydrogenation in Processes (a) 3 and (b) 4. White and orange spheres represent H and Mg, respectively. Blue spheres represent the atomic H involved in the reaction. (c and d) Energy changes of the second-layer atomic H during the dehydrogenation in Processes (c) 3 and (d) 4.

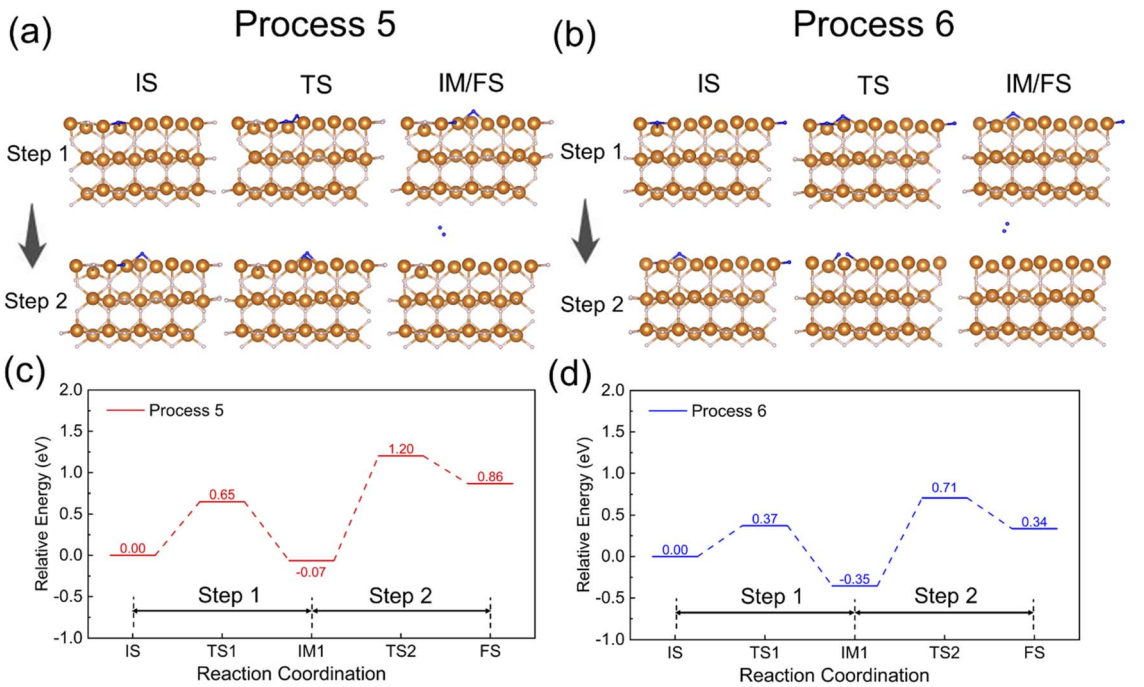

Fig. 4 (a and b) Top view of the initial structures of Processes (a) 5 and (b) 6. (c and d) The energy changes of the second-layer atomic H during the dehydrogenation in Processes (c) 5 and (d) 6. White and orange spheres represent H and Mg, respectively. Blue spheres represent the atomic H involved in the reaction.

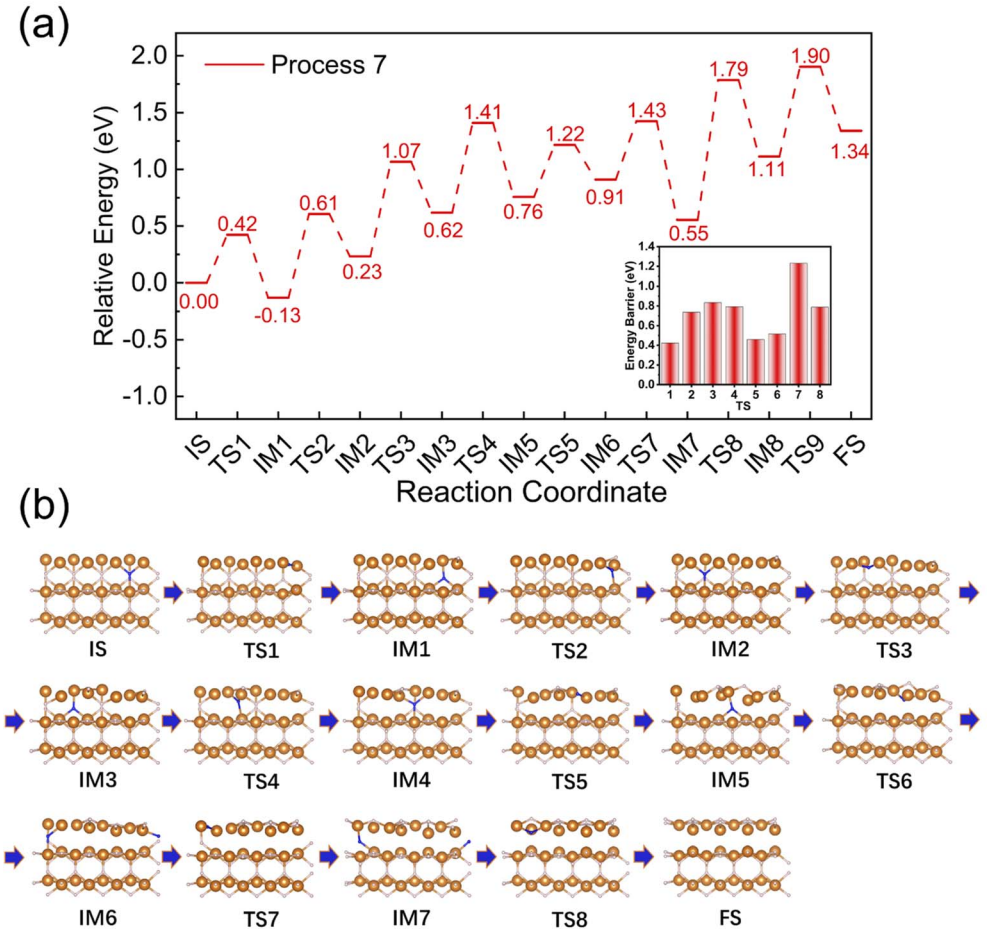

Fig. 5 (a) The third-layer H migration energy changes in Process 7. (b) Structure changes of the third-layer H migration in Process 7. White and orange spheres represent H and Mg, respectively. Blue spheres represent the atomic H involved in the reaction.

first layer (2.52–2.53 eV) through the same desorption path. Because a H vacancy appears at the SBH position when the second layer atomic H desorbs, similarly, the H migration barriers in Processes 3 and 4 are also higher than those of the first layer. Among them, the initial H migration barrier is the smallest (0.12 eV), which is almost identical to the results obtained by Du *et al.* (0.14 eV).[57] Note that there is only one FBH vacancy in their previous study, while our FBH vacancy concentration is 100%, indicating that the migration barrier of SBH is independent of the number of FBH vacancies. However, the subsequent migration barrier of SBH is much greater than 0.12 eV, indicating that the SBH migration barrier to BH is related to the vacancy at SBH. Note that the surface H vacancy concentration is 100%, while the second layer has no H vacancy; the surface of MgH_2 is equivalent to that shown in Fig. S2a.† Because the surface without SBH has a higher surface formation energy (Table S1†), SBH will migrate to the FBH position and form a more stable structure. After that, H vacancies appear in the second layer, but the migration energy barrier is still smaller than the dehydrogenation barrier.

To maintain the structural stabilities, the atomic H at the SBH and FBH positions react to achieve hydrogen desorption when 50% of the SBH vacancies appear. The number of H migration steps will be reduced because dehydrogenation does not require two atomic H at the FBH position. Similarly, the dehydrogenation sequence of SBH in Processes 5 and 6 will be changed to form a stable final structure (Fig. 1c). Fig. 1c illustrates that hydrogen desorption barriers in the second layer (1.06–1.51 eV) are smaller than those of the first layer (Fig. 4c and d). Moreover, the H migration barrier is also smaller than the desorption barriers in Processes 4 and 5. Therefore, it can be concluded that when the atomic H in the first layer can successfully desorb, the migration and desorption of the hydrogen in the second layer can happen much more easily, which is an interesting "burst effect" in MgH_2 dehydrogenation.

3.3 The third layer

After dehydrogenation of the two layers above, there is no atomic H in the second layer. Therefore, atomic H in the third layer need to migrate to the second layer before desorption. As a result, all SBHs can migrate to the second layer, and the migration barriers are 0.42–1.23 eV (Fig. 5a and b). According to the calculations, the H migration barrier of the third layer exceeds the previously calculated dehydrogenation barrier of this layer. Previous studies

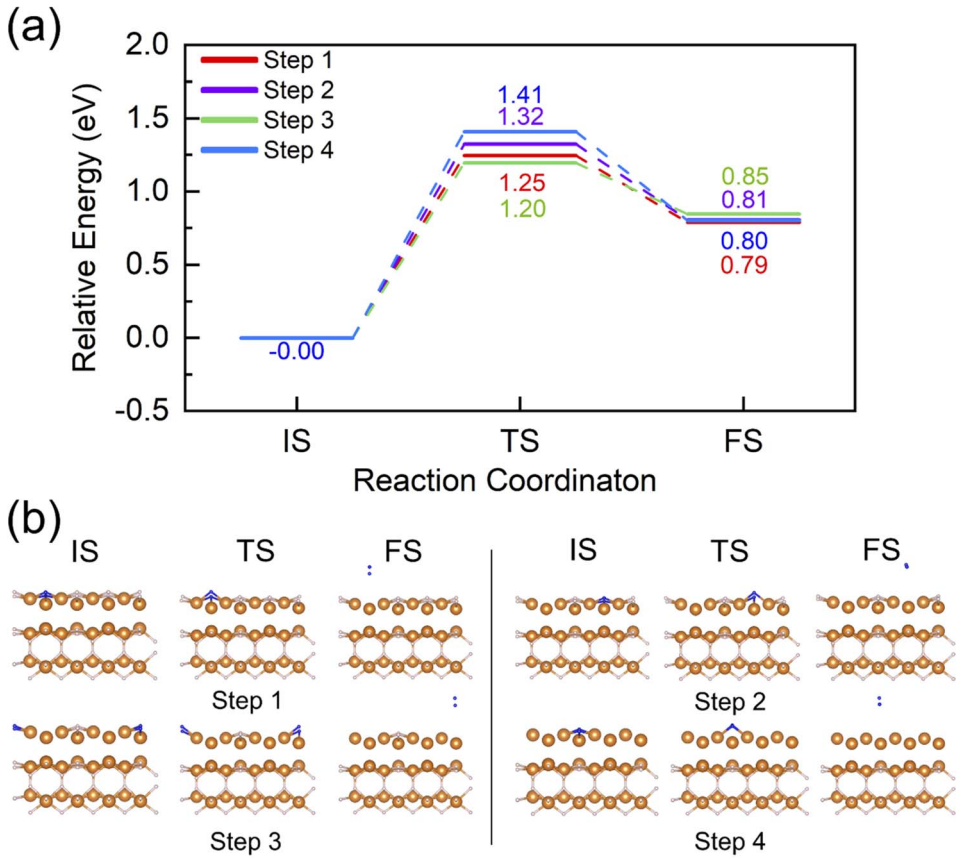

Fig. 6 (a) Energy changes of the third-layer atomic H during the dehydrogenation in Process 8. (b) Structural changes of the third-layer atomic H during Process 8. White and orange spheres represent H and Mg, respectively. Blue spheres represent the atomic H involved in the reaction.

proposed that for the H migration from the third to second layer, there are two different migration paths (0.45 and 0.66 eV).[57] The changes in the H vacancy in the second and third layers lead to a fluctuation in the height of the migration barrier.

According to the dehydrogenation of the above two layers, there are two dehydrogenation paths (FBH–FBH and SBH–FBH) for the atomic H migrating to the second layer. However, neither of the two dehydrogenation paths is applicable (Fig. S3†). Therefore, the two atomic H at the SBH position will directly combine (Fig. 6b) to form a feasible reaction path. Based on the calculations, the dehydrogenation barrier changes slightly (0.21 eV) with the desorption of H (Fig. 6a). All reaction barriers in this part are still lower than the hydrogen desorption barrier in the first layer.

3.4 Comparison of the three layers

Subsequently, the dehydrogenation kinetics and reaction barriers of the atomic H of the three layers were calculated (Table S2†). Note that the zero-point energy corrections and entropy were considered for all our calculations (Tables S3–S5†). After tallying all reaction energy barriers into violin diagrams (Fig. 7), only the desorption of the atomic H in the first layer has a relatively high energy barrier, while the H migration energy barriers in the second and third layers are smaller than the

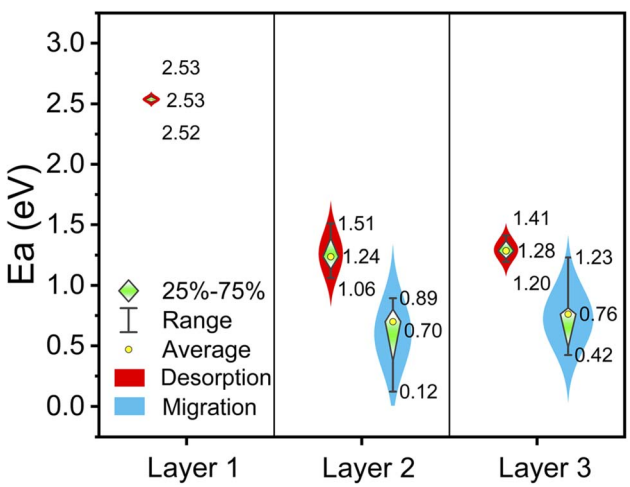

Fig. 7 Comparison of the three-layer atomic H migration and dehydrogenation energy barriers.

dehydrogenation energy barriers. Due to the low energy barrier in the subsequent H migration and desorption processes, once the surface atomic H acquires sufficient energy, the atomic H close to the surface will continuously desorb from MgH_2 (110).

3.5 Electronic analysis

The above calculations indicate that the dehydrogenation of atomic H in the first layer is rather special during the whole dehydrogenation. Inspired by this, we employed the COHP method[33,34] to analyze the electronics and energetics of various Mg–H bonds. The integrated crystal orbital Hamilton population (ICOHP) of the Mg–H bonds involved in the H_2 desorption process were calculated (Tables S6–S21†). The −ICOHPs of each bond (Fig. 8a–d) were calculated to analyze the change of Mg–H bond strength more clearly. As can be seen in Fig. 8a, the strengths of the Mg–H bonds in the first layer change slightly after dehydrogenation. The strengths of Bonds 1–6 and 1–7 increase with the decreasing intensity of Bonds 1–5 and 1–8. This may be responsible for the similar dehydrogenation barriers of Processes 2 and 1. With dehydrogenation, the strengths of most of the Mg–H bonds decreased. Reduction of Mg–H bond strengths will lead to the continuous reduction of the energy required for H migration and desorption, thus leading to the burst effect of MgH_2 dehydrogenation.

It can be found from the curve during the desorption of atomic H in the second layer that an −ICOHP value of about 0.7 appears in the BH bond that has been formed (the value of Processes 1 and 2 is ~0.9), making H desorb from Mg more easily (Fig. 8b and c). After that, the bonding strength in the third layer of Process 4 began to decrease. Therefore, the subsequent H migration still maintains a low energy barrier. For the atomic H of the second layer in the third stage of dehydrogenation (Process 8), the bonding strength decreases with the continuous dehydrogenation of MgH_2. The bonding strength of the new Mg–H bond formed after migration is also lower than that of the initial bond at the same position. To determine the Mg–H bonds related to the reaction region, we compared all bond strengths before and after the dehydrogenation of the first layer (Fig. S4†). When the FBHs were all desorbed, the majority of the first and second layers showed a decrease in the Mg–H bond strength. In contrast, the third layer remained largely unchanged. Therefore, the change of Mg–H bond strength in the reaction region reflects the change of the dehydrogenation energy barrier to a certain extent. The Mg–H bonds two or more layers away from the reaction region are less related to the reaction energy barrier. However, the energy barrier does not always decrease, indicating that the dehydrogenation energy barrier is not only related to −ICOHP, but also affected by the ambient environment. Moreover, the energy barrier change caused by the bond strength and the neighborhood environment may be the reason why nano MgH_2 and ball-milled MgH_2 can quickly solve the dehydrogenation problem.[58–61]

Based on the analysis above, the dehydrogenation performance of MgH_2 was significantly improved after the desorption of surface atomic H. To further explain the electronic changes after dehydrogenation, we analyzed four sets of ELFs of MgH_2 formed by two BHs reactions (Fig. 9a and b). The red color corresponds to a high degree of electron localization, while the blue color corresponds to a low electron density in this region. From the ELF results, the electron localization of near-surface H is relatively high (Fig. 9a). However, when the initial surface H desorbs from the MgH_2 surface (Fig. 9b) the electron

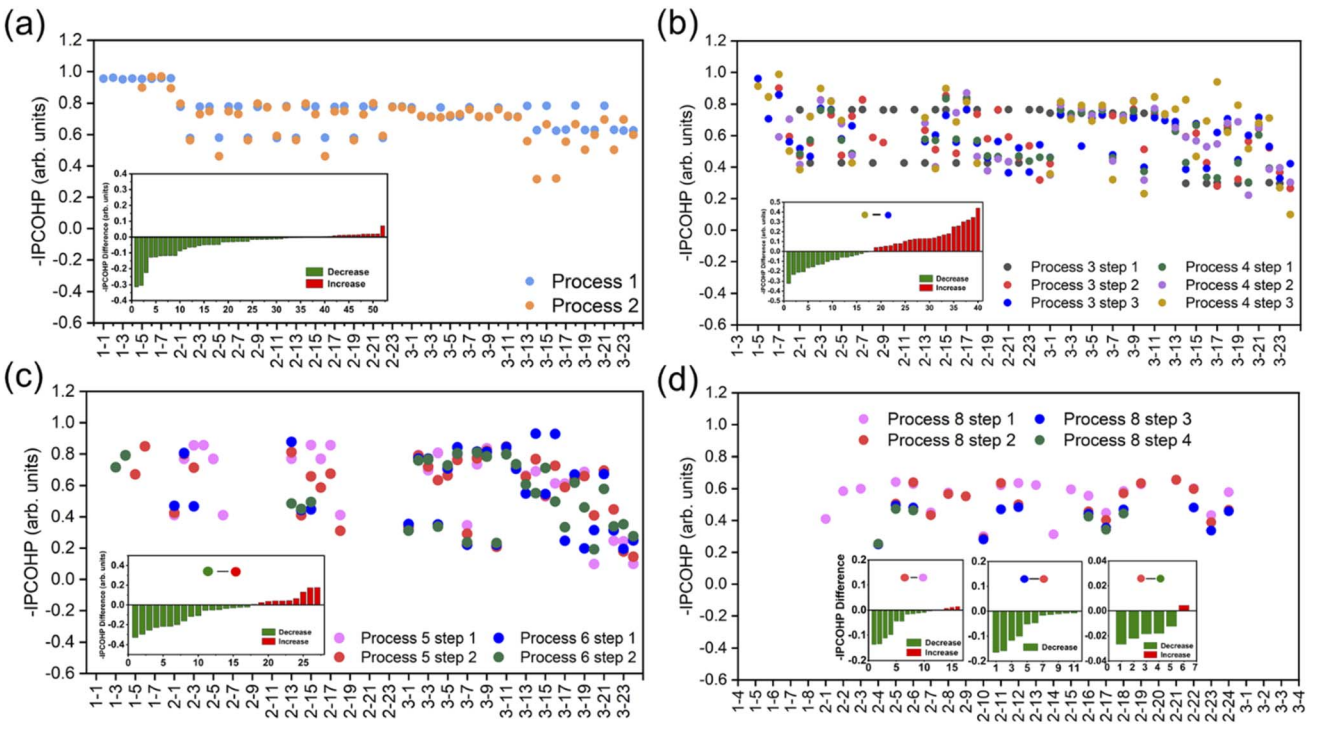

Fig. 8 The ICOHP of Mg–H bonds. The inset graphs show the difference in the bond strength of the desorption process (sorted from large to small). (a–d) Comparison of the Mg–H bonding strengths of (a) Processes 1 and 2, (b) Processes 3 and 4, (c) Processes 5 and 6, and (d) Process 8.

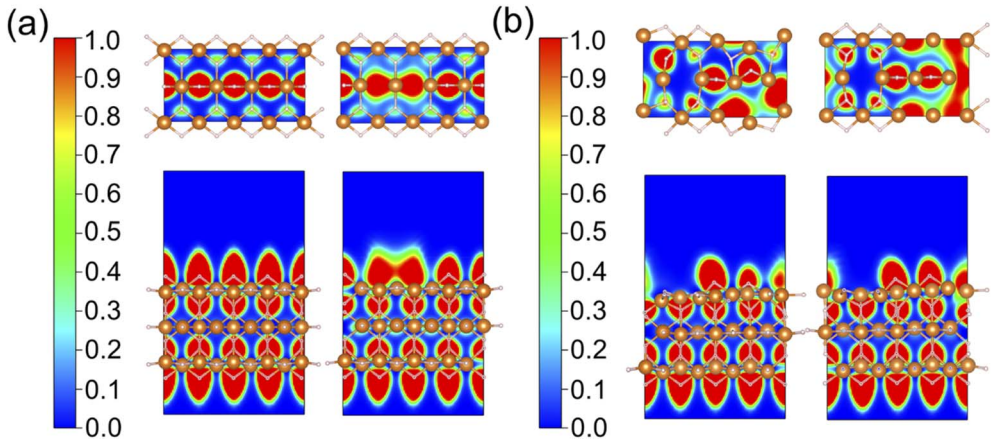

Fig. 9 The calculated ELFs of MgH_2. (a) ELF before the dehydrogenation in Processes 1 and 2 (the first layer). (b) ELF before the dehydrogenation in Processes 3 and 4 (the second layer).

localization of H migrated from the second-layer atomic H decreased at the same position. Interestingly, when a pair of surface atomic H desorb and form the H vacancies, there is still a considerable electron localization region at the vacancies (Fig. 9a). Because of this, the electron localization of another pair of atomic H is hardly changed. After the loss of surface H, the phenomenon disappears. Therefore, this phenomenon forces the dehydrogenation of the first layer atomic H to

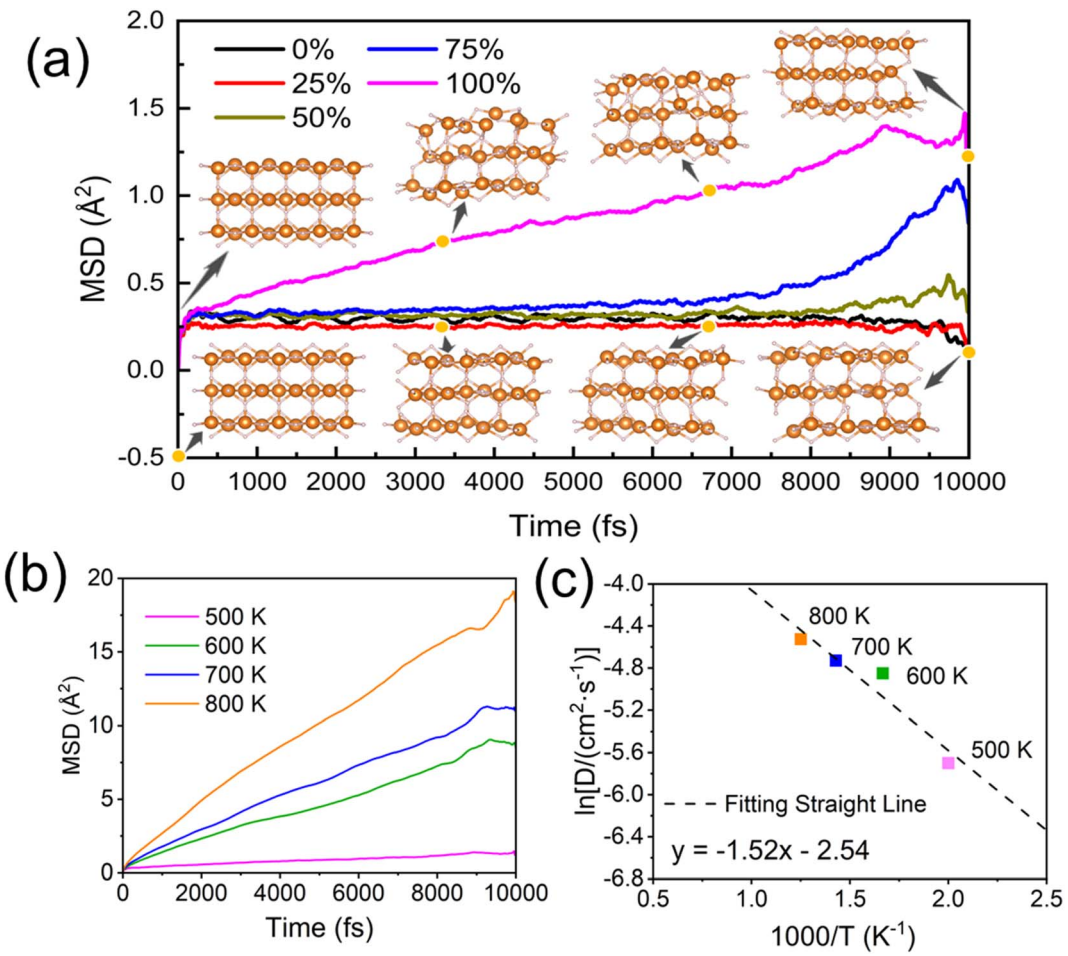

Fig. 10 (a) AIMD simulations on MgH_2 (110) before and after surface H loss. Yellow dots are the selected points of MgH_2 before (0%) and after (100%) surface H loss at 500 K. White and orange spheres represent H and Mg, respectively. (b) The MSD changes of atomic H at different temperatures when the H vacancy concentration is 100%. (c) The H migration barriers estimated by AIMD simulations.

maintain a high energy barrier. After all surface atomic H desorb, the degree of electron localization in this region drops sharply, resulting in a burst effect.

3.6 AIMD simulations

It can be clearly seen from the change in the energy barrier that dehydrogenation becomes much easier after MgH_2 (110) loses surface hydrogen. To further confirm whether its dehydrogenation kinetics have improved after initial dehydrogenation, we employed AIMD simulations to compare MgH_2 with and without surface atomic H for 10 ps. Previous MD simulations found that MgH_2 dehydrogenates only when the temperatures are above 663 K.[62] To compare the effects of different FBH vacancy concentrations on MgH_2, the calculated temperature should be lower than the dehydrogenation temperature of MgH_2. Therefore, we set a temperature of 500 K in AIMD simulations, which can observe obvious changes in diffusivity caused by the change in the H vacancy concentration. The structures with 0%, 25%, 50%, 75%, and 100% H vacancies were analyzed by changing the number of atomic H on the MgH_2 (110) surface. As expected, there is a large difference in the mean square displacements (MSDs), as shown in Fig. 10a. Atomic H will only tend to diffuse when the MSD shows an obvious linear growth after a slight relaxation. If the relaxation and stabilization stages of molecules are neglected, only the MgH_2 without surface atomic H has an obvious increase. It means that after the loss of all the surface atomic H, the atomic H of MgH_2 is inclined to diffuse, and therefore, the dehydrogenation kinetics can be significantly improved. By comparing the structures at 0, 3333, 6666, and 10 000 fs during AIMD simulations (Fig. 10a and S5a–c†), we found that the structures of MgH_2 (110) with BH are stable at 500 K. For the structure after surface H desorption, Mg and H are stabilized after a period of diffusion. It is worth noting that the SBH of the second layer migrates to the FBH position at 9000 fs, which is consistent with the predicted H migration mode of the second-layer atomic H.

Subsequently, we analyzed the diffusion trend of H in MgH_2 at 500, 600, 700, and 800 K (Fig. 10b) based on the Arrhenius equation and estimated its activation energy. The simulation object is a structure with a surface H vacancy rate of 100%, obtained from the above AIMD simulations. First, we estimated the diffusivity according to RMSDs at different temperatures (Fig. S6†). The fitting interval is the part that has a linear upward trend without obvious fluctuation, which does not include the relaxation stage. Then, the energy barrier was predicted using diffusivity and temperature (Fig. 10c). The H migration barrier in this structured state is 0.131 eV, similar to the value calculated by the CI-NEB method (0.12 eV). These provide further evidence of the burst effect in MgH_2 dehydrogenation.

4 Conclusion

In summary, we have analyzed the layer-by-layer dehydrogenation (*i.e.*, hydrogen desorption and atomic H migration) of a MgH_2 (110) model. The dehydrogenation barrier continuously changes with the formation of H_2 and diffusion of atomic H. Importantly, the initial H_2 desorption energy barriers are 2.52–2.53 eV, significantly higher than the subsequent H_2 desorption and H migration energy barriers. We found that for a stable MgH_2 (110) surface, surface H desorption is the most sluggish step in MgH_2 dehydrogenation because the H vacancy formed by first layer dehydrogenation has higher electron localization. AIMD simulations suggested that atomic H in the bulk diffuses only after the complete desorption of surface H. In addition, we found that the Mg–H bond strength continuously reduces with the progress of dehydrogenation, which accelerates H migration and desorption from subsequent layers. This phenomenon, which we assigned as the "burst effect", provides a solution to the slow dehydrogenation kinetics of MgH_2 and offers essential guidance for designing novel MgH_2-based composites for efficient hydrogen storage: promoting the initial dehydrogenation of MgH_2 by surface engineering (*e.g.*, doping)[52,63,64] could be the key to facilitating hydrogen desorption.

Conflicts of interest

There are no conflicts to declare.

Acknowledgements

This work was supported by the Interdisciplinary Innovation Program of North China Electric Power University (Grant Number XM2112355). Li Wei and Hao Li acknowledge the University of Sydney under the International SDG Collaboration Program.

References

1 L. Schlapbach, A. Züttel, P. Gröning, O. Gröning and P. Aebi, *Appl. Phys. A: Mater. Sci. Process.*, 2001, **72**, 245–253.
2 P. Jena, *J. Phys. Chem. Lett.*, 2011, **2**, 206–211.
3 Z. Ding, *Prog. Chem.*, 2021, **33**, 1586.
4 M. H. Mendelsohn, D. M. Gruen and A. E. Dwight, *Nature*, 1977, **269**, 45–47.
5 Z. Ding, H. Li and L. Shaw, *Chem. Eng. J.*, 2020, **385**, 123856.
6 B. Bogdanović, K. Bohmhammel, B. Christ, A. Reiser, K. Schlichte, R. Vehlen and U. Wolf, *J. Alloys Compd.*, 1999, **282**, 84–92.
7 A. C. Dillon, K. Jones, T. Bekkedahl, C. Kiang, D. Bethune and M. Heben, *Nature*, 1997, **386**, 377–379.
8 C. Liu, Y. Fan, M. Liu, H. Cong, H. Cheng and M. S. Dresselhaus, *Science*, 1999, **286**, 1127–1129.
9 N. S. Norberg, T. S. Arthur, S. J. Fredrick and A. L. Prieto, *J. Am. Chem. Soc.*, 2011, **133**, 10679–10681.
10 X. Zhang, Y. Liu, X. Zhang, J. Hu, M. Gao and H. Pan, *Mater. Today Nano*, 2020, **9**, 100064.
11 Z. Ding, Y. Lu, L. Li and L. Shaw, *Energy Storage Mater.*, 2019, **20**, 24–35.
12 F. Schüth, B. Bogdanović and M. Felderhoff, *Chem. Commun.*, 2004, 2249–2258.
13 W. Grochala and P. P. Edwards, *Chem. Rev.*, 2004, **104**, 1283–1316.

14 W. Li, C. Li, H. Ma and J. Chen, *J. Am. Chem. Soc.*, 2007, **129**, 6710–6711.
15 G. Liang, J. Huot, S. Boily, A. Van Neste and R. Schulz, *J. Alloys Compd.*, 1999, **291**, 295–299.
16 C. Shang and Z. Guo, *J. Power Sources*, 2004, **129**, 73–80.
17 R. Varin, T. Czujko and Z. Wronski, *Nanotechnology*, 2006, **17**, 3856.
18 N. Hanada, T. Ichikawa and H. Fujii, *J. Phys. Chem. B*, 2005, **109**, 7188–7194.
19 K.-F. Aguey-Zinsou, J. A. Fernandez, T. Klassen and R. Bormann, *Int. J. Hydrogen Energy*, 2007, **32**, 2400–2407.
20 J. J. Vajo, F. Mertens, C. C. Ahn, R. C. Bowman Jr and B. Fultz, *J. Phys. Chem. B*, 2004, **108**, 13977–13983.
21 A. Ranjbar, M. Ismail, Z. Guo, X. Yu and H.-K. Liu, *Int. J. Hydrog. Energy*, 2010, **35**, 7821–7826.
22 L.-P. Ma, X.-D. Kang, H.-B. Dai, Y. Liang, Z.-Z. Fang, P.-J. Wang, P. Wang and H.-M. Cheng, *Acta Mater.*, 2009, **57**, 2250–2258.
23 V. Bhat, A. Rougier, L. Aymard, X. Darok, G. Nazri and J. Tarascon, *J. Power Sources*, 2006, **159**, 107–110.
24 C. Wu, P. Wang, X. Yao, C. Liu, D. Chen, G. Q. Lu and H. Cheng, *J. Phys. Chem. B*, 2005, **109**, 22217–22221.
25 X. Yu, Z. Yang, H.-K. Liu, D. Grant and G. S. Walker, *Int. J. Hydrog. Energy*, 2010, **35**, 6338–6344.
26 J. Dai, Y. Song and R. Yang, *J. Phys. Chem. C*, 2010, **114**, 11328–11334.
27 J. Dai, Y. Song and R. Yang, *Int. J. Hydrog. Energy*, 2011, **36**, 12939–12949.
28 E. German, V. Verdinelli, C. R. Luna, A. Juan and D. Sholl, *J. Phys. Chem. C*, 2014, **118**, 4231–4237.
29 E. German, C. Luna, J. Marchetti, P. Jasen, C. Macchi and A. Juan, *Int. J. Hydrog. Energy*, 2014, **39**, 1732–1739.
30 L. Matović, N. Novaković, S. Kurko, M. Šiljegović, B. Matović, Z. K. Popović, N. Romčević, N. Ivanović and J. G. Novaković, *Int. J. Hydrogen Energy*, 2009, **34**, 7275–7282.
31 W.-Y. Chen, J.-J. Tang, Z.-W. Lu, M.-X. Huang, L. Liu, C.-C. He and Y.-J. Zhao, *Surf. Sci.*, 2021, **710**, 121850.
32 A. J. Du, S. C. Smith, X. D. Yao and G. Q. Lu, *Surf. Sci.*, 2006, **600**, 1854–1859.
33 V. L. Deringer, A. L. Tchougréeff and R. Dronskowski, *J. Phys. Chem. A*, 2011, **115**, 5461–5466.
34 R. Dronskowski and P. E. Bloechl, *J. Phys. Chem.*, 1993, **97**, 8617–8624.
35 P. E. Blöchl, *Phys. Rev. B: Condens. Matter Mater. Phys.*, 1994, **50**, 17953.
36 J. Wellendorff, T. L. Silbaugh, D. Garcia-Pintos, J. K. Nørskov, T. Bligaard, F. Studt and C. T. Campbell, *Surf. Sci.*, 2015, **640**, 36–44.
37 G. Kresse and D. Joubert, *Phys. Rev. B: Condens. Matter Mater. Phys.*, 1999, **59**, 1758.
38 J. P. Perdew, K. Burke and M. Ernzerhof, *Phys. Rev. Lett.*, 1996, **77**, 3865.
39 G. Kresse and J. Furthmüller, *Phys. Rev. B: Condens. Matter Mater. Phys.*, 1996, **54**, 11169–11186.
40 S. Grimme, J. Antony, S. Ehrlich and H. Krieg, *J. Chem. Phys.*, 2010, **132**, 154104.
41 A. D. Becke and E. R. Johnson, *J. Chem. Phys.*, 2005, **122**, 154104.
42 M. Zhu, Y. Lu, L. Ouyang and H. Wang, *Materials*, 2013, **6**, 4654–4674.
43 J. Zhang, Z. Li, Y. Wu, X. Guo, J. Ye, B. Yuan, S. Wang and L. Jiang, *RSC Adv.*, 2019, **9**, 408–428.
44 Y. Wang and Y. Wang, *Prog. Nat. Sci.: Mater. Int.*, 2017, **27**, 41–49.
45 G. Henkelman and H. Jónsson, *J. Chem. Phys.*, 2000, **113**, 9978–9985.
46 G. Henkelman, B. P. Uberuaga and H. Jónsson, *J. Chem. Phys.*, 2000, **113**, 9901–9904.
47 S. Maintz, V. L. Deringer, A. L. Tchougréeff and R. Dronskowski, *J. Comput. Chem.*, 2013, **34**, 2557–2567.
48 S. Maintz, V. L. Deringer, A. L. Tchougréeff and R. Dronskowski, *J. Comput. Chem.*, 2016, 1030–1035.
49 V. Wang, N. Xu, J.-C. Liu, G. Tang and W.-T. Geng, *Comput. Phys. Commun.*, 2021, **267**, 108033.
50 J. Kubečka, F. Uhlík and P. Košovan, *Soft Matter*, 2016, **12**, 3760–3769.
51 Y. Mo, S. P. Ong and G. Ceder, *Chem. Mater.*, 2012, **24**, 15–17.
52 Q. Li, S. Qiu, C. Wu, K. T. Lau, C. Sun and B. Jia, *J. Phys. Chem. C*, 2021, **125**, 2357–2363.
53 L.-L. Wang and D. D. Johnson, *J. Phys. Chem. C*, 2012, **116**, 7874–7878.
54 E. M. Kumar, A. Rajkamal and R. Thapa, *Sci. Rep.*, 2017, **7**, 1–11.
55 C. Liu, Q. Li, J. Zhang, Y. Jin, D. R. MacFarlane and C. Sun, *J. Mater. Chem.*, 2019, **7**, 4771–4776.
56 E. M. Kumar, A. Rajkamal and R. Thapa, *Sci. Rep.*, 2017, **7**, 15550.
57 A. Du, S. C. Smith and G. Lu, *J. Phys. Chem. C*, 2007, **111**, 8360–8365.
58 W. Zhu, L. Ren, C. Lu, H. Xu, F. Sun, Z. Ma and J. Zou, *ACS Nano*, 2021, **15**, 18494–18504.
59 L. Ren, W. Zhu, Y. Li, X. Lin, H. Xu, F. Sun, C. Lu and J. Zou, *Nano-Micro Lett.*, 2022, **14**, 1–16.
60 Z. Jia, B. Zhao, Y. Zhao, B. Liu, J. Yuan, J. Zhang, Y. Zhu, Y. Wu and L. Li, *J. Alloys Compd.*, 2022, 166853.
61 B. Liu, B. Zhang, H. Huang, X. Chen, Y. Lv, Z. Li, J. Yuan and Y. Wu, *J. Magnesium Alloys*, 2021, 2213–9567.
62 M. Lakhal, M. Bhihi, A. Benyoussef, A. El Kenz, M. Loulidi and S. Naji, *Int. J. Hydrogen Energy*, 2015, **40**, 6137–6144.
63 Q. Li, M. Yan, Y. Xu, X. L. Zhang, K. T. Lau, C. Sun and B. Jia, *J. Phys. Chem. C*, 2021, **125**, 8862–8868.
64 S. Dong, C. Li, E. Lv, J. Wang, H. Liu, Z. Gao, W. Xiong, Z. Ding, W. Yang and H. Li, *J. Mater. Chem.*, 2022, **10**, 19027–19045.

